Supporting Information

3D Printing Carbon-Carbon Composites With Multilayered Architecture for Enhanced Multifunctional Properties

Dharneedar Ravichandran[a], Anna Dmochowska[b], Barath Sundaravadivelan[c], Varunkumar Thippanna[a], Emile Motta de Castro[d], Dhanush Patil[a], Arunachalam Ramanathan[e], Yuxiang Zhu[a], Taylor Sobczak[e], Amir Asadi[f], Jorge Peixinho[b], Guillaume Miquelard-Garnier[b], and Kenan Song[e]

[a]School of Manufacturing Systems and Networks, Ira A. Fulton Schools of Engineering, Arizona State University, Mesa, AZ, USA 85212

[b]Laboratoire PIMM, UMR 8006, Arts et Métiers Institute of Technology, CNRS, CNAM, Hesam University, 151 boulevard de L'Hôpital, 75013, Paris, France

[c]Department of Mechanical Engineering, School for Engineering of Matter, Transport, and Energy, Ira A. Fulton Schools of Engineering, Arizona State UniversityArizona State University, Tempe, AZ, USA 85281

[d]J. Mike Walker '66 Department of Mechanical Engineering, Texas A&M University, College Station, Texas 77843, United States

[e]School of Environmental, Civil, Agricultural, and Mechanical Engineering (ECAM), College of Engineering, University of Georgia, Athens, Georgia, USA 30602

[f]Department of Engineering Technology and Industrial Distribution, Texas A&M University, College Station, Texas 77843-3367, United States
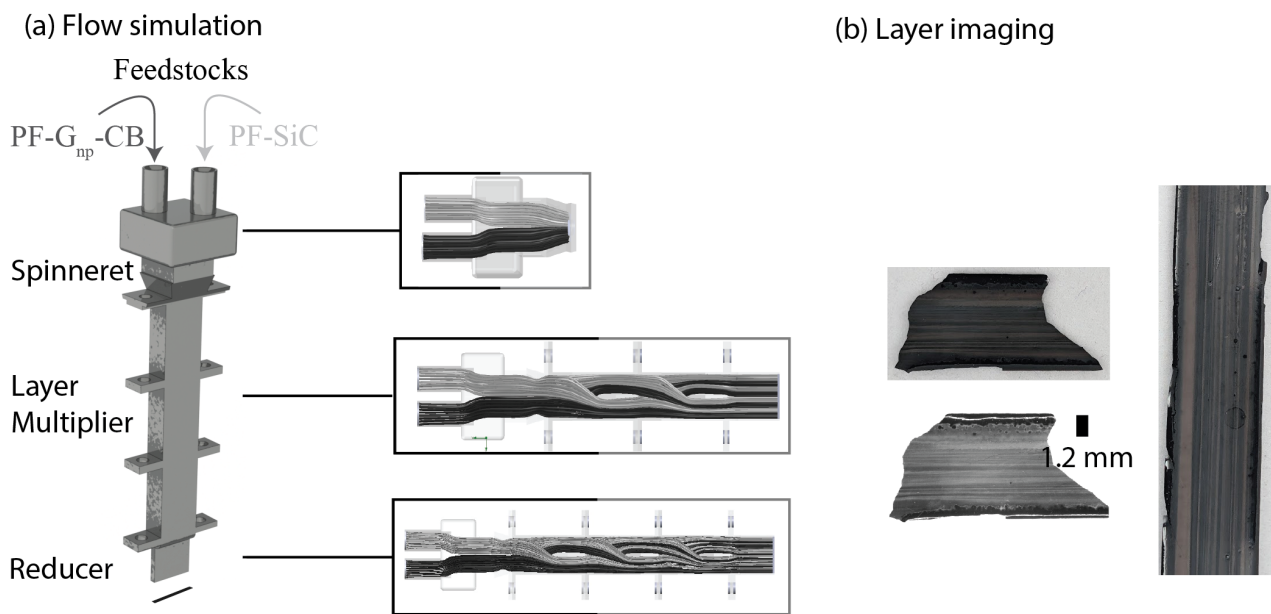
(a) Flow simulation

Feedstocks

PF-G$_{np}$-CB   PF-SiC

Spinneret

Layer
Multiplier

Reducer

(b) Layer imaging

1.2 mm

Figure S1: (a) The flow dynamics simulation of double feedstock processing (i.e., PF_SiC and PF_G$_{np}$-CB as the feedstocks in each printhead channel) with an example of three multipliers in the printhead to produce 16 layers in each printing line and (b) high dynamic range photographs and optical images of as-printed samples showing the distinct layers.
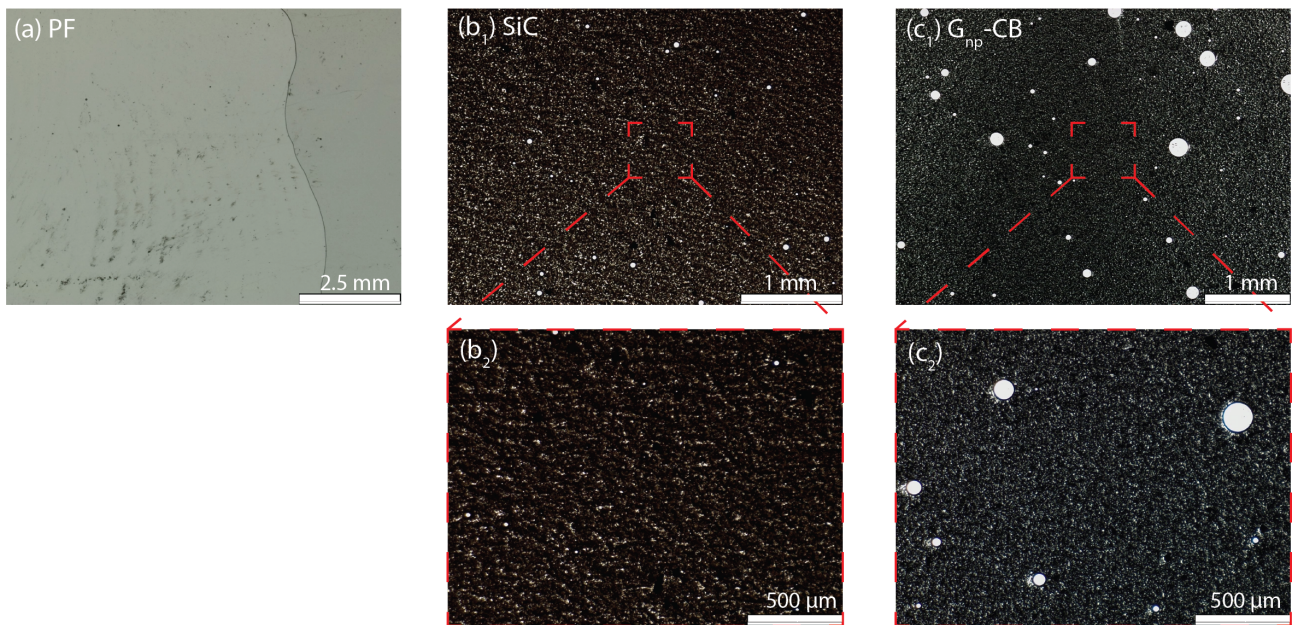
Figure S2: Dispersion of nanoparticle in the matrix (a) PF resin with no dispersion, (b$_1$-b$_2$) dispersion of SiC in PF, and (c$_1$-c$_2$) dispersion of G$_{np}$-CB in PF.
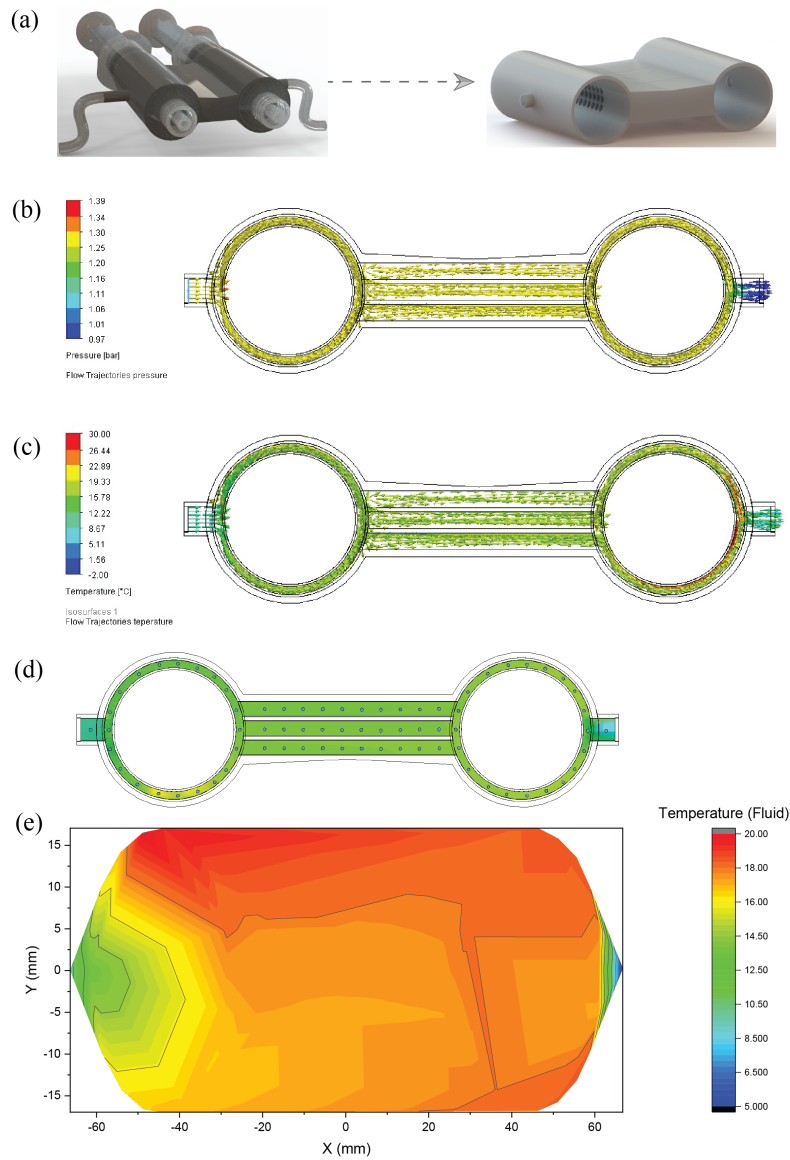
Figure S3: (a) Design of the air cooling setup, (b) contour image showing the pressure of the flowing air inside the setup, (c) contour image showing the temperature of the flowing air inside the setup, (d) highlighting the data collection points, and (e) showing a contour graph to visualize the temperature at each data points represented in d.

The flow simulation was done using SolidWorks flow Xpress on the air cooling setup (without a syringe). The internal surface temperature of the air cooling setup was considered to be 30°C with the airflow from left to right. The air pressure, temperature, and flow speed were gathered during the experiment and included as simulation control parameters.
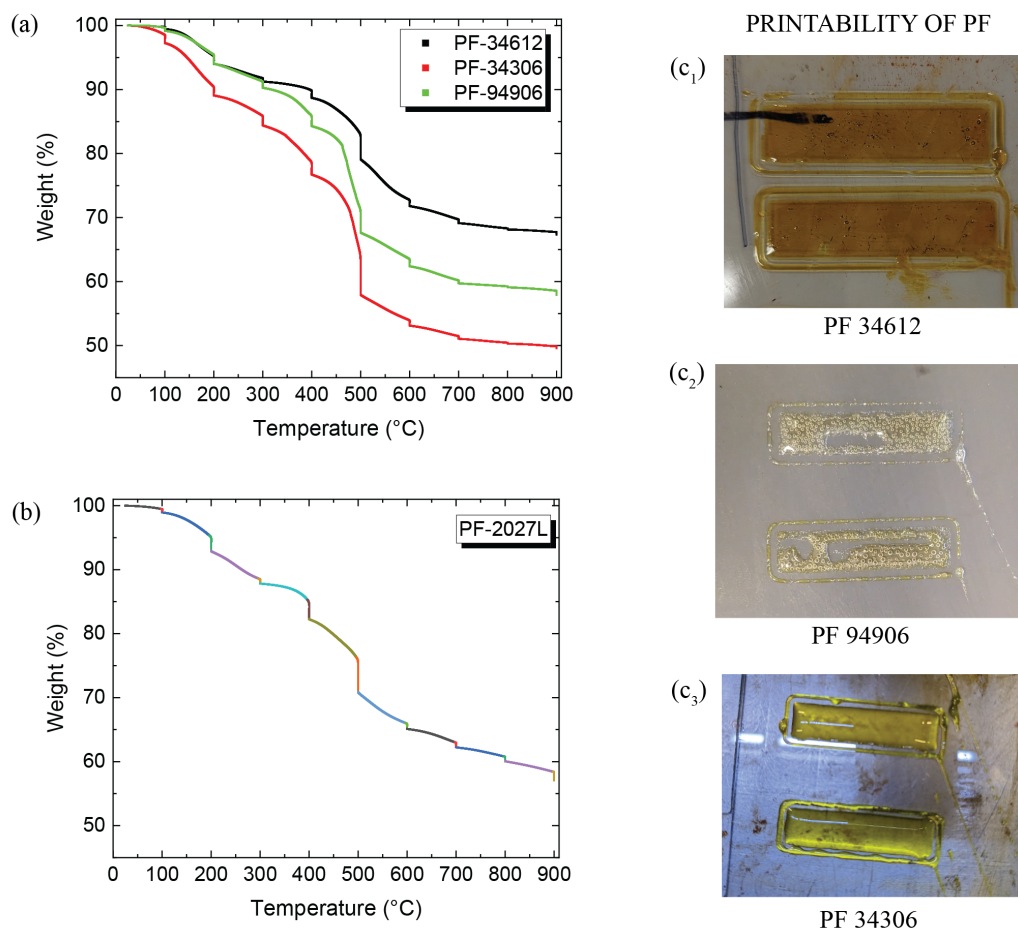
Figure S4: TGA analysis of commercially available (a) PF34612, PF34306, and PF94906, (b) PF2027L; printability of (c_1) PF34612, (c_2) PF94906, and (c_3) PF34306.

The TGA was programmed from room temperature (RT) to 900°C with an isotherm of 10 mins at every 100°C to predict the weight loss (**Figure S4a and b**). This also helped in understanding and finalizing the maximum carbonization temperature. The printability of the resins was also evaluated as seen in **Figure S4c$_1$-c$_3$**. Phenolic resins PF 34612 and 34306 were printable on a glass substrate but had a strong adhesion making it impossible to remove them without breaking. While phenolic resin 94906 had no structural integrity of the printed structure. Therefore phenolic resin PF2027L was chosen for conducting the experiments.
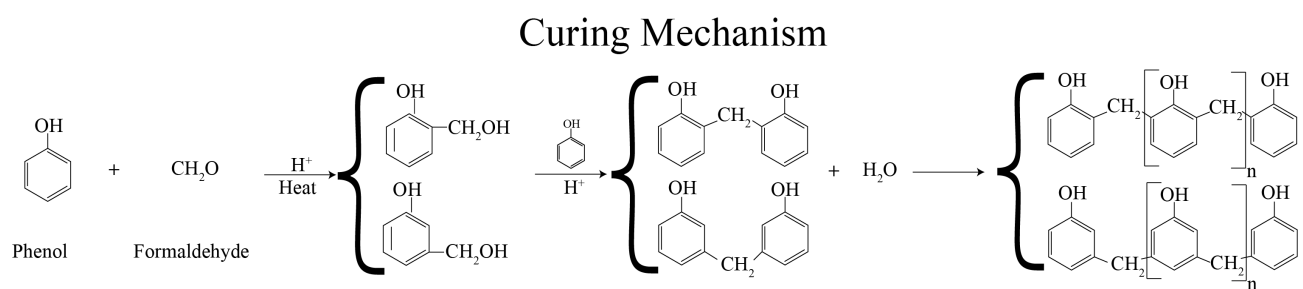
Curing Mechanism

Figure S5: Chemical equation displaying the curing mechanism of PF resins when subjected to heat.
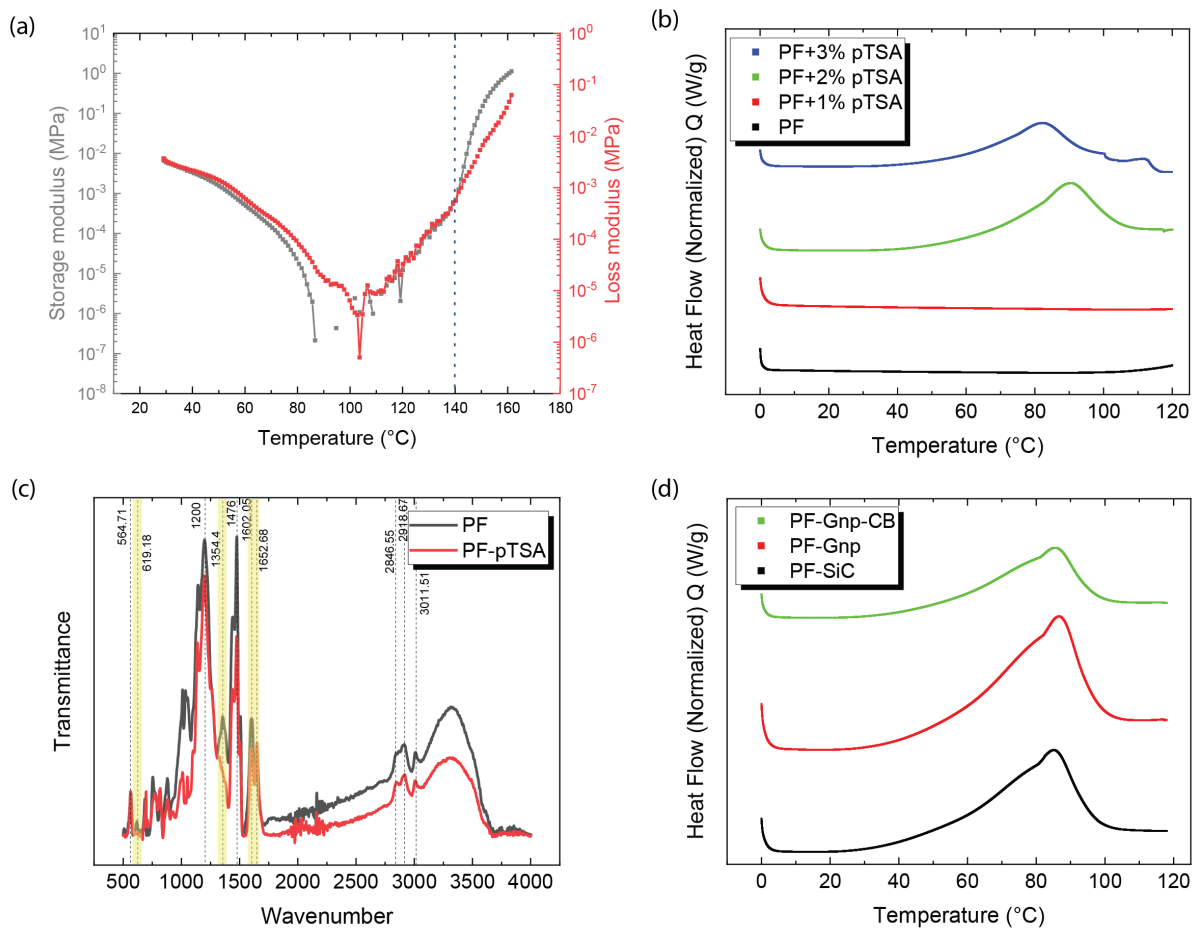
Figure S6: (a) Temperature sweep rheological test to predict the curing temperature of pristine PF resin, (b) DSC analysis of PF resin with and without catalyst (pTSA) to predict the curing temperature, (c) FTIR analysis to show the crosslinking of PF resin due to addition of pTSA. The highlighted regions in the graph show a new peak at 619.18 and 1354.4, while a peak disappearance at 1652.68 suggesting potential crosslinking to changes in the bonding of atoms, and (d) DSC analysis of PF resin with nanoparticle dispersion and 3 wt% pTSA to evaluate the curing temperature.

7
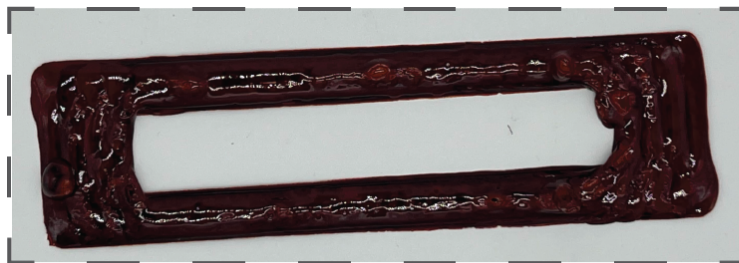
Figure S7: Photographs of as-printed PF resin with pTSA with respective wait time to show the surface finish of the final product.

Table S1: Evaluation of curing temperature for various feedstocks samples with addition of pTSA through DSC analysis.

Sample	pTSA conc. (%)	Onset Temp. (°C)	Enset Temp. (°C)	Peak Temp. (°C)	Enthalpy J/g
PF	0	–	–	–	–
PF	1	–	–	–	–
PF	2	70.66	103.06	90	84.74
PF	3	62.38	91.93	81.96	48.65
PF-SiC	3	57.97	96.41	85.06	160.86
PF-G_{np}	3	59.65	96.87	86.54	199.09
PF-G_{np}-CB	3	58.65	95.70	85.47	104.76

(a) Perfect Sample - without porosity
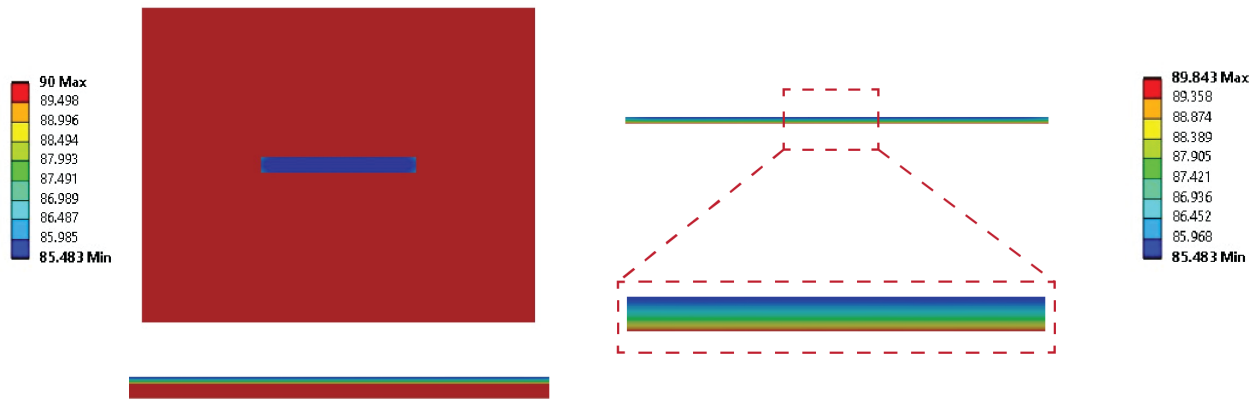
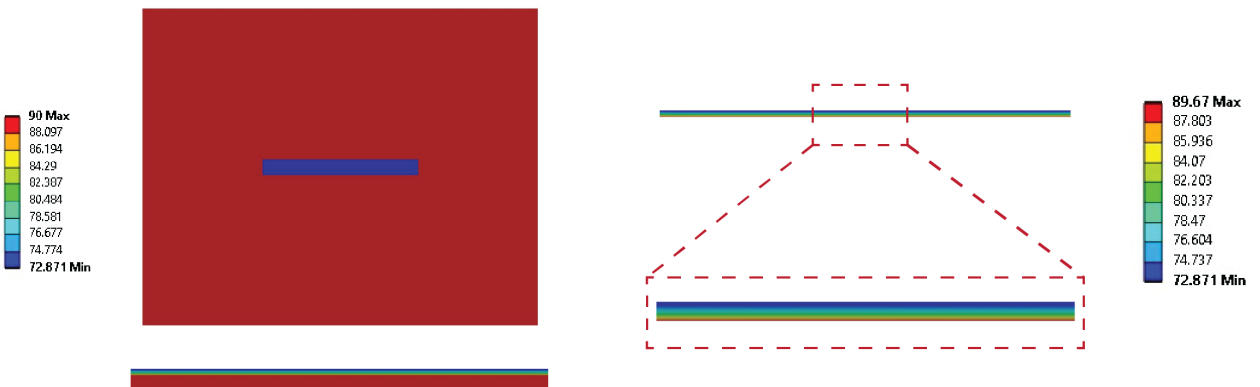(b) With porosity

Figure S8: Transient thermal analysis of deposited PF resin on a print bed to evaluate the temperature in the Z-axis for (a) PF sample without porosity and (b) PF sample with assuming a porosity of 50%

The transient thermal analysis was performed using Ansys Workbench replicating the deposition of PF resin on the print bed during the 4D printing process. Material data were used directly from the vendor's material data sheet for the PF resin. The material data for the print which is made of aluminum and a glass substrate were used from the Ansys engineering database. Two simulations with (50%) and without porosity were done as represented in **Figure S8a and b**. The simulation helped in understanding the resin heat flux/ propagation upon deposition to print multiple layers in the Z-axis. The simulation was done for 3 minutes, which is the total time taken to print a ladder structure as shown in Figure 3 of the manuscript.
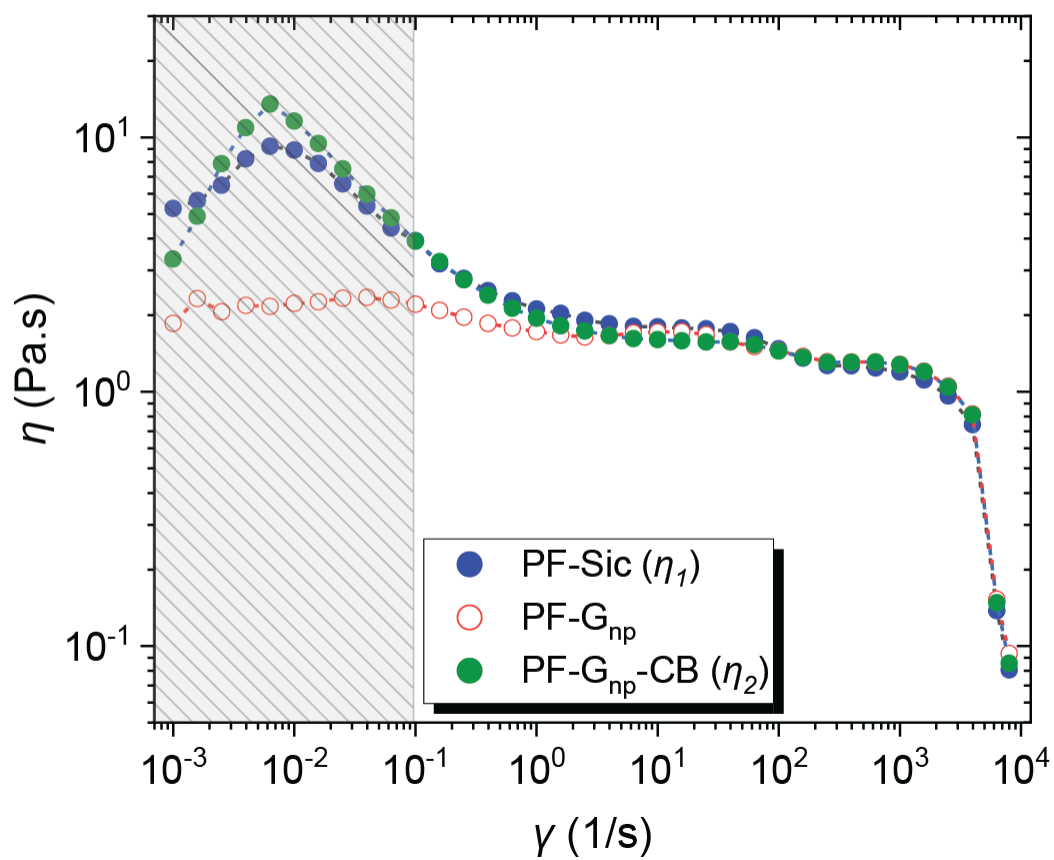
Figure S9: Flow sweep rheology of PF resin with dispersion to identify and achieve the necessary viscosity similarity. Note: Figure 2a in the manuscript has the same data curves of PF-SiC and PF-G_{np}-CB. This graph justifies the including of CB as a viscosity with comparison to PF-G_{np}.
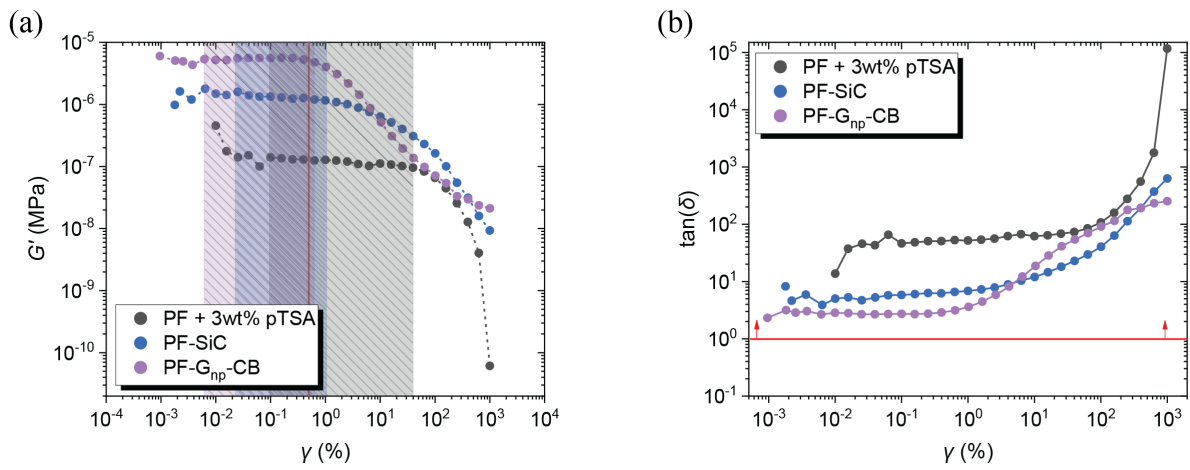
Figure S10: (a) Amplitude sweep of the feedstocks to identify the LVER and (b) tanδ of the respective feedstocks obtained through a frequency sweep.

Table S2: Thermo-mechanical (T.- mech.) properties of C-C composites through conventional manufacturing from literature.

Composition		Heat treatment (°C)	Temperature (°C)	Coating	T.- mech. Modulus (GPa)	Ref
A	B					
Pitch PAN Rayon	CF	3000	RT - 2400	No	13 @ RT, 25 @ 1600 26 @ RT, 36 @ 1600 17 @ RT, 27 @ 1600	1
SiC	PyC CF	1000	RT - 2300		125 @ RT, 200 @ 1000	2
SiC	PyC CF	1000	RT - 2600		90 @ RT, 140 @ 1000	3
PF	PAN CF	2600	150 - 2600		1.35 @ 150, 0.2 @ 1800	4
TiC	PAN CF	2100	RT - 1400		0.6 @ RT, 0.44 @ 1400	5
CF	CF	1200	RT - 1500	SiSiC	76.5 @ RT, 78 @ 1500	6
PF	CF CF/0.5wt% GNP CF/1.5wt% GNP CF/3wt% GNP CF/5wt% GNP	800	RT	No	1.23 @ RT 1.91 @ RT 2.83 @ RT 2.11 @ RT 2.08 @ RT	7
CF	SiC	1400	RT		22.6 @ RT	6
PF	CF	1000 2200	50 - 450		3.84 @ 50, 3.65 @ 450 2.06 @ 50, 2.12 @ 450	8
PF	**−** **Gnp-CB** **SiC** **M**	**1250**	**RT - 500**		**6.3 @ RT, 1 @ 200** **4.6 @ RT, 7.52 @ 500** **4.33 @ RT, 9.5 @ 300** **7.5 @ RT, 9.36 @ 400**	**This work**

TABLE NOTE: The table represents the minimum and maximum achievable modulus. For more details refer to the literature cited. It is crucial to clarify that the mechanical properties of our carbon-carbon composites, which utilize non-continuous fillers such as graphene nanoplatelets-carbon black (Gnp-CB), silicon carbide (SiC), and metallic additives (M), should not be directly compared with those composites reinforced by continuous carbon fibers. Continuous fibers, such as those used in the referenced literature, typically offer superior mechanical properties due to their continuous nature and the resulting load transfer efficiency within the composite material. In our work, the discon-

tinuous nature of the fillers leads to different reinforcement mechanisms, which are better described by composite mechanics models that take into account the impact of particle size, distribution, and the interface between the matrix and the filler. For instance, models like the Rule of Mixtures may oversimplify the behavior of our composites, whereas more complex models like the Halpin-Tsai equations provide a more accurate representation by considering the geometry and orientation of dispersed particles. Therefore, while our fillers impart significant improvements in specific properties relevant to their applications—evidenced by the enhanced thermal and mechanical stability at elevated temperatures—comparisons to continuous fiber composites should acknowledge these fundamental differences in composite architecture and the resulting mechanical behavior.

Section S1

C-C composites have emerged as a solution to the demand for materials capable of withstanding extreme conditions while retaining exceptional mechanical properties. As a result, their thermo-mechanical characteristics have been extensively studied. However, due to the wide array of material combinations possible in creating these composites, direct comparisons can be challenging. Table R1 provides a comprehensive overview of the various material combinations typically used in the conventional manufacturing of C-C composites.

Historically, PF resins have been explored as potential matrix materials in C-C composites. Nonetheless, carbon fiber (CF) has often been preferred due to its well-established properties and extensive study within the realm of C-C composites. It's worth noting that CF has been a staple choice for many due to its excellent properties.

In recent years, there has been a growing interest in exploring other carbon-based materials such as graphene nanoplatelets (GNP) and silicon carbide (SiC) to achieve unique properties in C-C composites. These materials offer distinct advantages and properties that can further enhance the overall performance of the composite.

In traditional manufacturing processes, such as repeated impregnation and carburization, efforts are made to reduce porosity, leading to improved properties in the final composite. However, these processes can be time-consuming and resource-intensive.

Our study marks a significant advancement in C-C composite manufacturing through the utilization of 3D printing technology. While the production time has been significantly reduced, our focus moving forward is to enhance the structural and composite properties of these materials. This research serves as a stepping stone towards perfecting the manufacturing processes of C-C composites, ultimately leading to the development of high-performance materials capable of meeting diverse industrial demands.

Table S3: Electrical properties of C-C composites through conventional manufacturing from literature.

Composition		Heat treatment	Temperature	Coating	Electrical		Ref
A	B	(°C)	(°C)		σ (S/cm)	ρ ($\mu\Omega$ m)	
PF	PAN-CF with green carbon	900		No	28.74 - 61.35	N/A	9
PF	PAN-CF	1500		Ni	72	N/A	10
Pitch	Recycled Cf	1000	RT		N/A	600	11
	Milled Cf					410	
	Powdered Cf					161.26	
PAN	CNT	2150			392	2600	12
PF	CF	2400		No	14.52	N/A	13
Pitch	PAN CF	3000			1180	N/A	14
Pitch	G-fiber	2750	1200 - 2700		N/A	820 - 920	15
PF	– **Gnp-CB** **SiC** **M**	**1250**	**RT - 500**		**1.7 @ RT, 0.7 @ 500** **3.6 @ RT, 3.3 @ 500** **4.9 @ RT, 4.3 @ 500** **3.6 @ RT, 4.6 @ 500**	**N/A**	**This work**

NOTE: The conductivity and resistivity values in the table represent the maximum achievable electrical properties irrespective of the concentration of nanoparticles. Refer to the literature cited for more details.

Section S2

Carbon possesses intrinsic electrical conductivity; however, the composite nature of C-C composites introduces complexities to this conductivity. Nevertheless, there is a growing interest in exploring the multifunctional behavior of C-C composites, extending beyond their thermal and mechanical properties.

Our comparative analysis in Table R2 underscores the significant influence of reinforcement type and carburization temperature on improving the electrical conductivity of C-C composites, with PAN-derived carbon fiber (PAN-CF) showcasing superior conductivity among the samples studied.

Literature reports have also shed light on the electrical properties of key reinforcing materials. Silicon carbide (SiC), for instance, has demonstrated an electrical conductivity range of 0.7 – 1.4 S/cm,[16] while graphene nanoplatelets (GnP) exhibit a higher conductivity of 5.5 S/cm.[17,18]

Although the thermo-electrical properties of C-C composites have not been extensively explored, SiC and graphene have garnered considerable attention in research circles. SiC is recognized as a p-type semiconductor, boasting a high Seebeck coefficient of 366.64 µV/K at 323 K and an impressive 564.40 µV/K at 923 K.[16,19] Meanwhile, graphene exhibits a lower Seebeck coefficient of 50 µV/K but compensates with excellent thermal transport properties, boasting a figure of merit (ZT) value ranging from 0.15 to 1, depending on its dimension.[18,20]

However, integrating these particles within a composite introduces complexities due to the composite's intricate internal structures. As a result, there is ongoing research to optimize their placement and interaction within the composite matrix to achieve maximum performance. These ongoing efforts underscore the continuous exploration and potential enhancements in the multifunctional properties of C-C composites.

References

[1] S. Sato, A. Kurumada, H. Iwaki and Y. Komatsu, *Carbon*, 1989, **27**, 791–801.

[2] T. Cheng, X. Wang, R. Zhang, Y. Pei, S. Ai, R. He, D. Fang and Y. Yang, *Journal of the European Ceramic Society*, 2020, **40**, 630–635.

[3] T. Cheng, *Journal of the European Ceramic Society*, 2021, **41**, 2335–2346.

[4] S. R. Dhakate and O. P. Bahl, *Carbon*, 2003, **41**, 1193–1203.

[5] G.-M. Song, Y. Zhou, S. Joong and L. Kang, *Materials and Design*, 2003, **24**, 639–646.

[6] Q. gang Fu, B. yi Tan, L. Zhuang and J. yi Jing, *Materials Science and Engineering: A*, 2016, **672**, 121–128.

[7] D. Bansal, S. Pillay and U. Vaidya, *Carbon*, 2013, **55**, 233–244.

[8] W. chi Chang and C. chi M Ma, *Dynamic mechanical properties of carbon-carbon composites*, 1995.

[9] R. Kumar, S. Varshney, K. K. Kar and K. Dasgupta, *Advanced Powder Technology*, 2018, **29**, 1417–1432.

[10] R. Kumar, K. K. Kar and K. Dasgupta, *Journal of Composite Materials*, 2021, **55**, 1733–1748.

[11] M. Zambrzycki, J. Tomala and A. F. Szczypta, *Ceramics International*, 2018, **44**, 19282–19289.

[12] Z. Zhou, X. Wang, S. Faraji, P. D. Bradford, Q. Li and Y. Zhu, *Carbon*, 2014, **75**, 307–313.

[13] B. Tang, Y. Wang, J. Yu, K. Yang, Y. Lu, X. Wu, K. Sun, X. Li, R. Fan, D. Shi and W. Shao, *Journal of Chemistry*, 2020, **2020**, 1–15.

[14] T. S. K. Raunija and N. Supriya, *Carbon Letters*, 2017, **22**, 25–35.

[15] A. Cezairliyan and A. P. Miiller, *Specific Heat Capacity and Electrical Resistivity of a Carbon-Carbon Composite in the Range 1500-3000 K by a Pulse Heating Method*, 1980.

[16] Y. Taki, M. Kitiwan, H. Katsui and T. Goto, *Journal of Asian Ceramic Societies*, 2018, **6**, 95–101.

[17] Y. Zare, K. Y. Rhee and S. J. Park, *Scientific Reports*, 2023, **13**, 1596.

[18] J. Wang, X. Mu and M. Sun, *The thermal, electrical and thermoelectric properties of graphene nanomaterials*, 2019.

[19] S. C. Ozer, K. Arslan and S. Turan, *Journal of the Australian Ceramic Society*, 2023.

[20] J. S. Yun, S. Choi and S. H. Im, *Advances in carbon-based thermoelectric materials for high-performance, flexible thermoelectric devices*, 2021.